Electrochemically Controlled Auger Quenching of Mn^{2+} Photoluminescence in Doped Semiconductor Nanocrystals

Michael A. White, Amanda L. Weaver, Rémi Beaulac, and Daniel R. Gamelin*

Department of Chemistry, University of Washington, Seattle, Washington 98195-1700, United States

ABSTRACT Auger processes in colloidal semiconductor nanocrystals have been scrutinized extensively in recent years. Whether involving electron—exciton, hole—exciton, or exciton—exciton interactions, such Auger processes are generally fast and hence have been considered prominent candidates for interpreting fast processes relevant to photoluminescence blinking and multiexciton decay. With recent advances in the chemistries of nanocrystal doping, increasing attention is now being paid to analogous photophysical properties of colloidal-doped semiconductor nanocrystals. Here, we report the first investigation of the effects of electron-dopant exchange interactions on dopant luminescence in doped semiconductor nanocrystals. Using electrochemical techniques, electrical control of charge-carrier densities in films of colloidal Mn^{2+}-doped CdS quantum dots has been achieved and used to demonstrate remarkably effective Auger de-excitation of photoexcited Mn^{2+}. The doped nanocrystals are found to be substantially more sensitive to Auger de-excitation than their undoped analogues, a result shown to arise primarily from the long Mn^{2+} excited-state lifetime. This observation of exceptionally effective Auger quenching has broader implications in areas of high-power, single-particle, or electrically driven luminescence of doped semiconductor nanocrystals, and also suggests interesting opportunities for modulating Mn^{2+} photoluminescence intensities on sublifetime time scales, or for imaging charge carriers in nanocrystal-based devices.

KEYWORDS: charged quantum dots · manganese-doped nanocrystals · photoluminescence · electrochemistry · cyclic voltammetry · auger de-excitation

Transition-metal and rare-earth ions serve as activators in numerous electroluminescent (EL) devices based on impact excitation.[1−3] In this process, a conduction-band (CB) electron accelerated by an electric field imparts some of its excess energy to excite a dopant ion (Figure 1a), which may then relax radiatively back to its ground state. Impact excitation has been proposed to underpin many Mn^{2+}-doped II—VI EL devices, including recently reported Mn^{2+}-doped nanocrystal EL devices prepared by soft processing.[4−8] The microscopic reverse of impact excitation is Auger de-excitation. In this process, energy is transferred from an excited dopant to a charge carrier to yield the ground-state dopant and an excited charge carrier (Figure 1b). Auger de-excitation can be a major nonradiative loss channel that ultimately limits the efficiencies of such EL devices.[9−12] Auger de-excitation also limits gain in SiO_2 optical wave guides containing both Er^{3+} ions and Si nanocrystals,[13] although Er^{3+} is not within the nanocrystals themselves.[14,15]

Advances in the chemistries of colloidal nanocrystal doping have recently provided access to entirely new forms of doped semiconductor nanostructures, and the rich physical properties displayed by such structures are now attracting broad interdisciplinary interest.[16−39] However, whereas electron—exciton and biexciton Auger de-excitation processes in undoped colloidal semiconductor nanocrystals have received tremendous attention,[40,41] partly in relation to multiexciton decay[42,43] and nanocrystal blinking,[44−48] analogous carrier-dopant and exciton-dopant Auger quenching processes in doped semiconductor nanocrystals have not yet been examined.[49] To the contrary, recent publications have suggested that Mn^{2+} PL is not affected by ionization of the nanocrystal host,[31] and that nonlinear PL power dependencies of doped nanocrystals can be interpreted in terms of biexciton Auger de-excitation[37] or Mn^{2+} excitation saturation[35] without consideration of Mn^{2+}-centered Auger de-excitation processes.

Here, we report the use of electrochemical techniques to control Mn^{2+} photoluminescence (PL) in Mn^{2+}:CdS quantum dot (QD) films. Introduction of CB electrons into these QDs is shown to very effectively quench Mn^{2+} PL by Auger de-excitation. Steady-state and time-resolved PL measurements performed as a function of charging allow the fundamental electron-Mn^{2+} Auger rate constant to be determined. Poor

* Address correspondence to Gamelin@chem.washington.edu.

Received for review March 7, 2011 and accepted March 31, 2011.

10.1021/nn200889q

carrier mobility is concluded to limit Auger quenching at extremely low charging levels. The exceptionally high sensitivity of Mn^{2+}-doped QDs to Auger de-excitation is shown to be associated primarily with the long Mn^{2+} excited-state lifetime. These results highlight the need to consider dopant-based Auger processes explicitly when interpreting excitation power dependence, blinking, and electroluminescence efficiencies from doped semiconductor nanocrystals.

RESULTS AND DISCUSSION

Colloidal Mn^{2+}-Doped CdS Quantum Dots. Figure 2a shows 295 K absorption, PL, and PL excitation (PLE) spectra of colloidal wurtzite 0.5% Mn^{2+}:CdS nanocrystals synthesized by modification of literature methods.[26] Owing to quantum confinement, the first excitonic absorption maximum occurs at 2.8 eV, ~0.3 eV higher than in bulk CdS, corresponding to an average QD diameter of $d_{QD} \approx$ 4.5 nm.[50] This diameter and Mn^{2+} concentration yield, on average, ~5 Mn^{2+}/QD. The PL spectrum is dominated by intense Mn^{2+} $^4T_1 \rightarrow {}^6A_1$ d–d luminescence centered at 2.10 eV, with a room-temperature quantum yield (QY) of 29%. The PLE spectrum collected monitoring this d–d PL (Figure 2a) confirms sensitization by the CdS host. No excitonic PL is observed, reflecting rapid energy transfer to Mn^{2+}.[36,51–53] Figure 2b shows a room-temperature electron paramagnetic resonance (EPR) spectrum of 0.5% Mn^{2+}:CdS QDs. The hyperfine splitting parameter A = (65.5 ± 0.2) × 10^{-4} cm^{-1} agrees well with that of bulk Mn^{2+}:CdS (65.3 × 10^{-4} cm^{-1}).[54] Figure 2c shows 5 K 0–6 T magnetic circular dichroism (MCD) spectra of a drop-coated film of 0.5% Mn^{2+}:CdS QDs. The lowest energy excitonic transition is characterized by strong positive intensity at its leading edge that follows the $S = {}^5/_2$ magnetization of Mn^{2+} (Figure 2c, inset). An excitonic Zeeman splitting energy at saturation of ΔE_{Zeeman}^{sat} = 13.2 meV is estimated[16] from these data, with a low-field 5 K g value of ~70, confirming the existence of giant excitonic Zeeman splittings dominated by Mn^{2+}-exciton sp–d exchange coupling.[16,55] X-ray diffraction (XRD) data (Figure 2d) confirm the wurtzite structure and show peak widths consistent with $d_{QD} \approx 4.5 \pm 0.5$ nm. Overall, these data confirm successful synthesis of the target Mn^{2+}:CdS QDs, which were then used in electrochemical experiments.

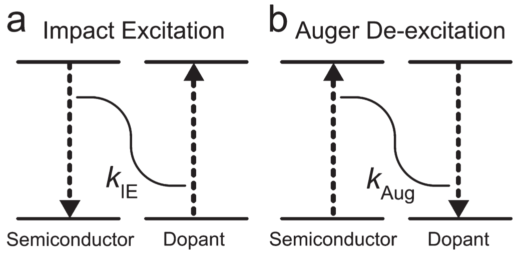

Figure 1. Impact excitation and Auger de-excitation processes. (a) Impact excitation of a dopant ion in a semiconductor involves nonradiative energy transfer from a highly energetic carrier to the dopant, yielding a relaxed carrier and the dopant in an electronic excited state. (b) Auger de-excitation of an excited dopant in a semiconductor involves nonradiative energy transfer from the dopant to a band carrier, yielding a relaxed dopant and a highly excited carrier. k_{IE} and k_{Aug} are the rate constants associated with impact excitation and Auger de-excitation, respectively. Auger de-excitation is the microscopic reverse of impact excitation.

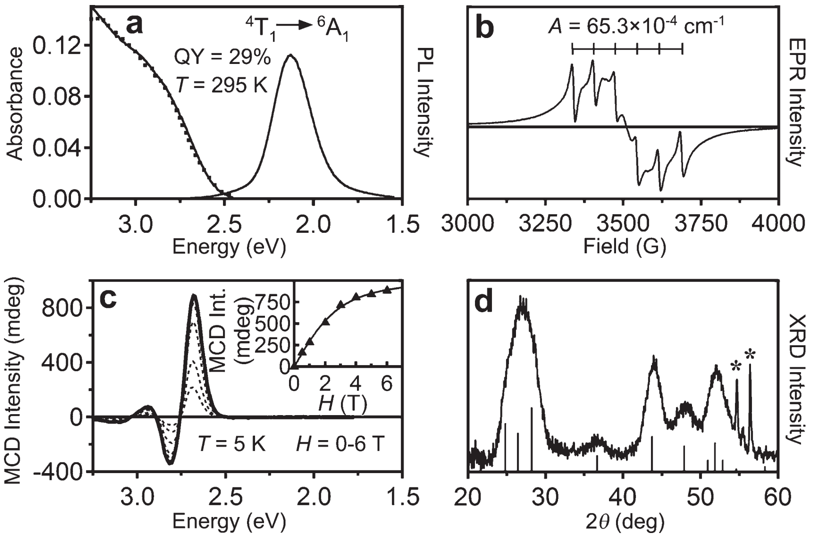

Figure 2. Colloidal Mn^{2+}:CdS quantum dots. (a) Room-temperature absorption (solid, left axis), photoluminescence (solid, right axis), and photoluminescence excitation (dashed, right axis) spectra of colloidal d_{QD} = 4.5 nm, 0.5% Mn^{2+}:CdS nanocrystals suspended in toluene. The PL quantum yield of the colloidal Mn^{2+}:CdS nanocrystals under nitrogen atmosphere is 29%. (b) Room-temperature EPR spectrum of colloidal d_{QD} = 4.5 nm, 0.5% Mn^{2+}:CdS QDs suspended in toluene, showing the characteristic six-line hyperfine pattern. The literature hyperfine coupling constant for Mn^{2+} in CdS is indicated.[54] (c) Variable-field (0–6 T), 5 K MCD spectra of a drop-coated film of colloidal d_{QD} = 4.5 nm, 0.5% Mn^{2+}:CdS QDs. The inset shows the field dependence of the MCD intensity at 2.66 eV (▲). The solid line plots the anticipated MCD magnetization curve (g_{Mn} = 2.0, $S = {}^5/_2$, and T = 5 K). (d) Powder XRD of d_{QD} = 4.5 nm, 0.5% Mn^{2+}:CdS nanocrystals. The literature powder diffraction intensities for wurtzite CdS are shown as black bars. The sharp peaks (*) are associated with the Si substrate.

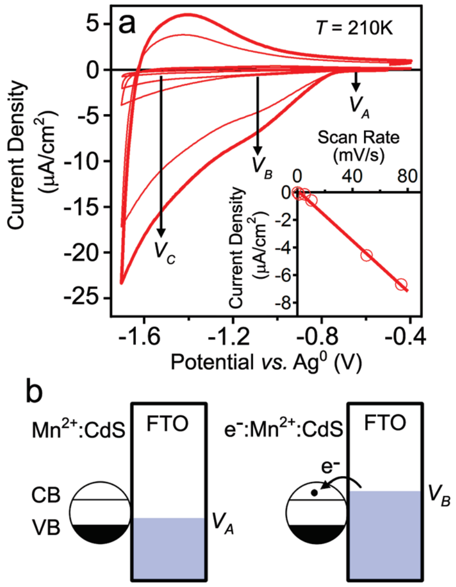

Figure 3. Cyclic voltammetry of a Mn^{2+}:CdS quantum dot film. (a) Cyclic voltammograms collected as a function of scan rate (ν) for a drop-coated film of d_{QD} = 4.5 nm, 0.5% Mn^{2+}:CdS QDs on FTO in a 0.1 M TBAP solution in DMF at 210 K (scan rates: 1, 5, 10, 50, and 75 mV/s). Points V_A, V_B, and V_C indicate the uncharged, reduction peak maximum (partial $1S_e$ filling), and completion of the first reduction wave (complete $1S_e$ filling, onset of $1P_e$ filling), respectively, as determined by absorption spectroscopy. (Inset) Scan rate dependence of the peak current measured at V_B. The asymmetry between forward and reverse scans is partly attributable to FTO, see Supporting Information. (b) Scheme for charging of Mn^{2+}:CdS quantum dots. At V_A, the energy gap between the Fermi level and the $1S_e$ levels in the CdS nanocrystal film is large, so there is no electron transfer. At V_B, electrons can tunnel into the film ($N_{e^-} \approx 1\ e^-_{CB}$/QD).

Electrochemical Reduction of Mn^{2+}-Doped Quantum Dots. Mn^{2+}:CdS QD films were prepared by depositing the above colloids onto 3-mercaptopropyl-trimethoxysilane (MPTMS) treated F^-:SnO_2 (FTO) electrodes and cross-linking with 1,7-heptanediamine following literature procedures.[41,56−58] Figure 3a shows cyclic voltammograms (CVs) of a representative Mn^{2+}:CdS QD film (thickness ≈ 200 nm), measured at 210 K. A reduction wave is observed at *ca.* −1.2 V *versus* Ag⁰. Similar reduction waves in undoped II−VI QDs have been interpreted as electron injection into the $1S_e$ CB levels of the nanocrystals.[56−59] The onset of a second reduction peak is observed at more negative potentials (Figure 3a) and tentatively interpreted as filling of the $1P_e$ CB levels.[58] The peak current density at the first reduction wave depends linearly on scan rate (Figure 3a, inset), consistent with reduction of adsorbed species.[60] Reoxidation is slow, so the observed oxidation wave is smaller than the reduction wave. This slow return is also present in control experiments with MPTMS-treated FTO substrates without QDs (see Supporting Information), and therefore does not come entirely from the nanocrystals themselves. Likewise, the FTO electrodes themselves also show current flow in this potential window, which likely contributes to the asymmetry between forward and reverse waves (see Supporting Information). Similar contributions from substrates appear to be generally observed in related literature studies.[57,61]

As in other QD films,[61] the exact potential of the first reduction wave differed for different films of the same QDs, and even drifted over extended times (tens of hours), presumably reflecting surface fluctuations and the use of an Ag⁰ pseudoreference. For comparison across samples, we therefore identify three special points in the CV that are common to all samples, as illustrated in Figure 3a. V_A denotes a potential far below any detectable charging, V_B denotes the peak potential of the first reduction wave (50% $1S_e$ filling, see below), and V_C denotes a potential after completion of the first reduction wave (complete $1S_e$ filling, onset of $1P_e$ filling). The electrode at potentials V_A and V_B is shown schematically in Figure 3b.

Figure 4a (top) shows the film's absorption spectrum measured as a function of applied potential. Increasing from V_A to V_C causes bleaching of the excitonic absorption at ∼2.8 eV, which recovers fully upon reoxidation. Figure 4a (bottom) shows the difference absorption spectra as a function of potential ($\Delta A/A = (A(V) - A(V_A))/A$, where A is the absorbance at 2.8 eV and at V_A). The peak in $\Delta A/A$ gradually shifts to higher energy with potential, because larger particles with lower $1S_e$ energies are generally reduced at lower potentials than smaller particles.[56,61,62] As the potential approaches V_C, the maximum change in $\Delta A/A$ converges to *ca.* −0.5, the remaining absorbance being attributed to broad higher energy excitonic transitions.[61] The bleach of the lowest excitonic level is thus reported using $\Delta A/A_0$, where $A_0 = A(V_A) - A(V_C)$ at 2.8 eV; by definition, $\Delta A/A_0$ ranges from 0 to −1. As in previous studies,[57,58,61] the bleach in excitonic absorption was used to measure N_{e^-}, the average number of $1S_e$ e^-/QD. V_B is defined as the potential at which $\Delta A/A_0 = -0.5$. At V_B, $N_{e^-} = 1.0\ e^-_{CB}$/QD. Identification of V_B is thus independent of the number of QDs or the film thickness, and does not rely on detailed knowledge of the QD extinction coefficients. Identification of V_B also does not rely on CV measurements, which generally overestimate the number of conduction-band electrons.[57,61] For example, using the time-integrated current of a potential sweep from V_A to V_B and the film thickness determined from its optical density,[50] an average of ∼1.5 e^-/QD is estimated at V_B in Figure 3a, consistent with partial filling of the $1S_e$ level[56,58] but greater than the number indicated by the optical data.

As with the colloids, the PL of films made from these QDs (*e.g.*, Figure 4b) is dominated by the Mn^{2+} $^4T_1 \rightarrow {}^6A_1$ transition, but a broad trap luminescence band is now observed, centered at ∼1.75 eV.[63] For the film shown in Figure 4b, the 295 K Mn^{2+} PL QY dropped from 29% to 6%. Similar QY losses have been reported for other

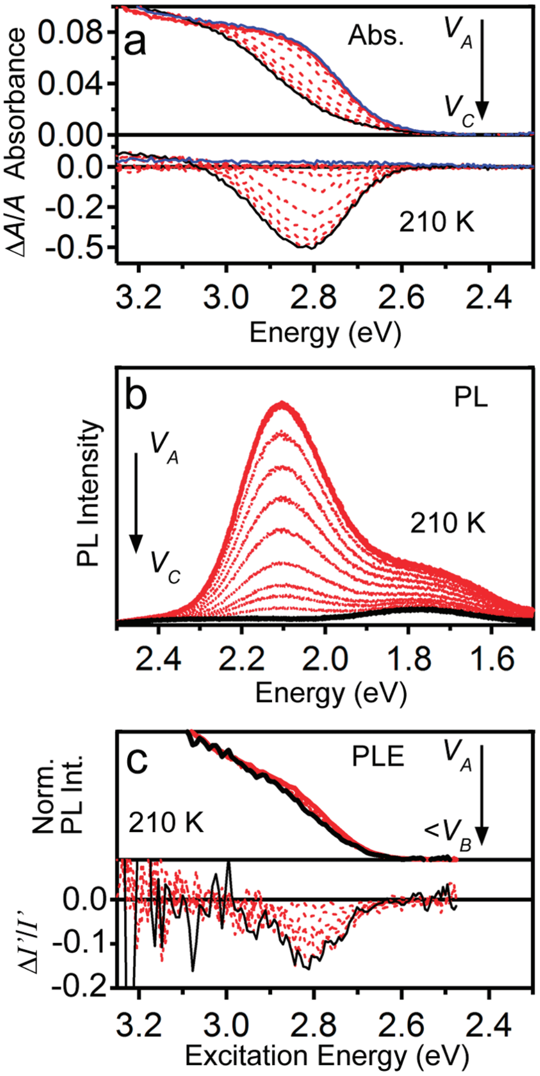

Figure 4. Optical response of a Mn^{2+}:CdS quantum dot film to electron injection. (a) (Top) 210 K absorption spectra collected at various potentials from V_A to V_C (red and black solid, respectively), and with the potential returned to V_A (blue solid). (Bottom) Difference absorption ($\Delta A/A$) spectra at various potentials. (b) 210 K photoluminescence (PL) spectra collected at various potentials from V_A to V_C (red and black solid, respectively). (c) (Top) 210 K photoluminescence excitation (PLE) spectra collected monitoring the integrated photoluminescence intensity between 2.0 and 2.5 eV, with potentials ranging from V_A (red solid) to below V_B (*i.e.*, −1.1 V in Figure 5a, black). The PLE curves were normalized at 3.03 eV. (Bottom) Difference PLE spectra at various potentials ($\Delta I'/I'$, where prime indicates intensities from normalized PLE spectra).

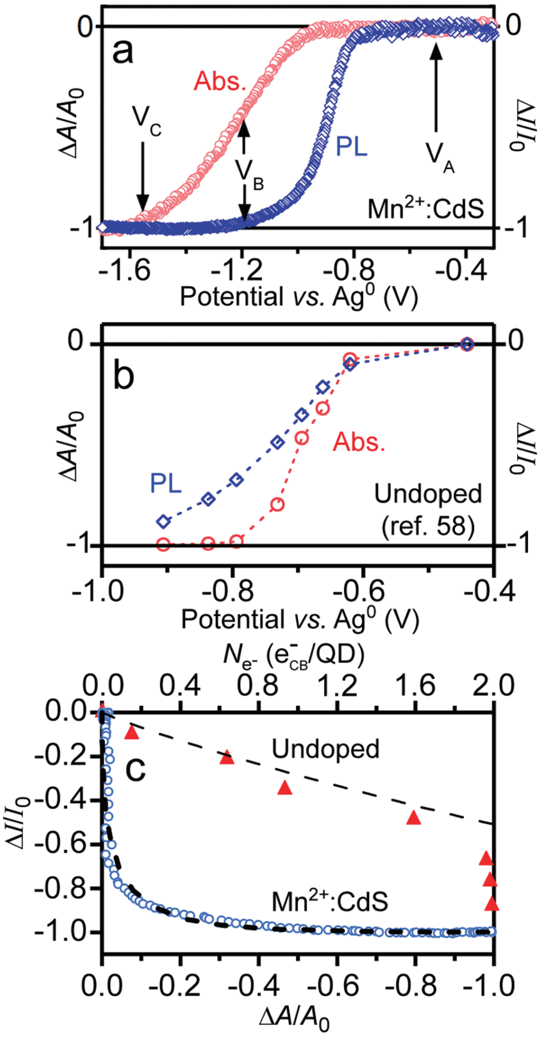

Figure 5. Comparison of doped and undoped QDs. (a) $\Delta A/A_0$ at 2.8 eV (red open circle) and $\Delta I/I_0$ integrated between 2.0 and 2.5 eV (diamond) for Mn^{2+}:CdS QDs, collected simultaneously during a linear sweep voltammogram (ν = 10 mV/s) at 210 K. (b) $\Delta A/A_0$ (red open circle) and $\Delta I/I_0$ (diamond) for undoped CdSe/CdS nanocrystals collected at room temperature in a similar electrochemical configuration, adapted from ref 58. (c) Plots of $\Delta I/I_0$ *vs* $\Delta A/A_0$ for undoped CdSe/CdS (red triangle, from ref 58) and Mn^{2+}:CdS (open circle) QDs. The dashed lines in panel c were calculated using eq 5 as described in the text.

nanocrystal films, for example dropping from ∼30% in CdSe/CdS colloids to ∼2% in a film.[58] The Mn^{2+} PL QY of this film was improved to 42% by lowering the temperature to 210 K, and all electrochemistry measurements were therefore performed at this temperature. With charging, the PL intensity decreases over the entire spectral range (Figure 4b). Interestingly, the Mn^{2+} PL intensity drops substantially faster than the trap emission with potential, suggesting that Mn^{2+} PL is more sensitive to CB electrons (*vide infra*). Both PL bands recover fully upon returning to V_A (see below). All films showed spectroelectrochemical properties similar to those seen in Figure 4b.

Figure 4c (top) shows PLE spectra collected at different potentials. To account for the overall PL decrease with charging, the PLE intensities have been normalized at 3.05 eV, where the absorbance does not change with potential. Like the absorption, the PLE intensity at the absorption edge also bleaches upon charging. A smaller overall difference is seen by PLE only because the range of potentials that can be sampled before the PL is entirely quenched is small. Quantitatively, the exciton's PLE bleach (Figure 4c, bottom) agrees well with its absorption bleach

(Figure 4a, bottom) at the same potential, for example, when $\Delta A/A = -0.16$, $\Delta I'/I' = -0.16$ (where $\Delta I' = I'(V) - I'(V_A)$ and I' is the exciton's PLE intensity when the PLE spectrum is normalized at 3.05 eV).

To quantify the difference between PL quenching and absorption bleaching, absorption and PL data were collected simultaneously for another Mn^{2+}:CdS QD film during the course of a linear sweep voltammogram (Figure 5a). Importantly, the Mn^{2+} PL intensity begins to drop well before any detectable absorption bleach. Although separated by ~0.32 V, the two responses are roughly parallel, with the PL curve being slightly steeper at low potentials. Mn^{2+} PL is quenched by ~75% ($\Delta I/I_0 = -0.75$) when excitonic absorption is bleached by only 3% ($\Delta A/A_0 = -0.03$), and it is quenched by 98% at V_B, where excitonic absorption is bleached by only 50%. This response is strikingly different from that of undoped CdSe/CdS QDs, where excitonic PL is quenched by only ~33% at V_B (Figure 5b).[58] This major qualitative difference between Auger quenching of doped and undoped QDs is emphasized by plotting $\Delta I/I_0$ *versus* $\Delta A/A_0$ for both in Figure 5c, and constitutes the central new observation of the present study.

It is conceivable that the vastly increased sensitivity of the Mn^{2+}-doped QDs to Auger quenching could be related to surface traps, but this possibility can be eliminated experimentally. Figure 6a shows the voltage dependence of the PL spectrum of a Mn^{2+}:CdS QD film prepared by heating the nanocrystal film for a shorter time after the ligand exchange, which reduces surface trap emission intensity by approximately a factor of 3 relative to the Mn^{2+} PL shown in Figure 4b, and by over a factor of 5 relative to the film used for the data in Figure 5a. With applied potential, Mn^{2+} PL quenching is again observed. The Mn^{2+} PL is fully recovered upon film reoxidation. Figure 6b plots $\Delta I/I_0$ and $\Delta A/A_0$ *versus* potential for this film as in Figure 5a. For easy comparison with the data from Figure 5a, the *x* axis is referenced to V_B (where $\Delta A/A_0 = -0.5$) and the data from Figure 5a are included on the same scale. The raw data are provided in Supporting Information. Notable from Figure 6b is the fact that the voltage difference between absorption and PL curves is essentially identical for the two samples (~0.32 V). The absorption and PL curves are again roughly parallel, a feature predicted by the Fermi-Dirac model discussed below, and elimination of surface traps makes the PL response to applied voltage sharper and more complete at lower potentials; that is, the electrochemical quenching of Mn^{2+} PL becomes *more* pronounced, not less pronounced as might be anticipated were traps responsible. The sharpening of the electrochemical response when traps are eliminated is interpreted as reduced Stark-effect broadening of the distribution of CB potentials. Overall, these results provide compelling experimental evidence against any pivotal role played by surface trap states in the electrochemical PL quenching of these Mn^{2+}-doped CdS nanocrystals. This conclusion is consistent with previous demonstrations that surface-trapped electrons are unable to effectively quench the excitonic luminescence of undoped QDs,[58] because the probability densities of the highly localized Mn^{2+} d wave functions at the QD surfaces are even smaller than those of the excitonic wave functions.

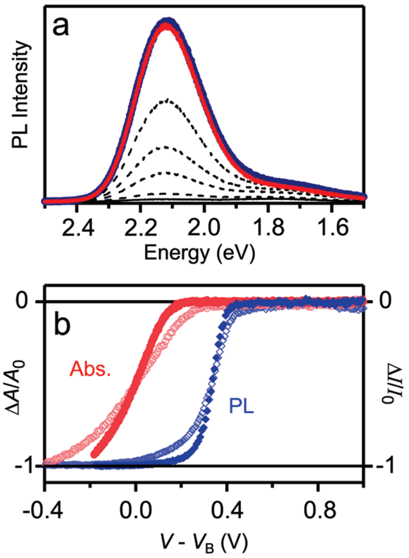

Figure 6. Comparison of Mn^{2+}:CdS QD films with different surface trap concentrations. (a) 210 K photoluminescence (PL) spectra collected at various potentials from V_A to V_C (red and black solid, respectively), for a film of Mn^{2+}:CdS QDs with minimal surface-trap PL. The surface trap PL intensity is decreased by over a factor of 5 relative to the film of Figure 5a (and by a factor of 3 relative to Figure 4b). The Mn^{2+} PL is quenched with applied potential, and is recovered upon film reoxidation (blue solid). (b) Voltage response of $\Delta A/A_0$ at 2.8 eV (solid red circle) and $\Delta I/I_0$ integrated between 2.0 and 2.5 eV (solid blue diamond) for the Mn^{2+}:CdS QDs from panel a, plotted *vs* $V - V_B$ to allow direct comparison with the data from Figure 5a (open red circle and open diamond). Although the shapes of the two data sets differ, the voltage difference between $\Delta A/A_0$ and $\Delta I/I_0$ curves is essentially identical (~0.32 V). Elimination of surface traps makes the electrochemical PL quenching more pronounced.

Time-resolved PL data were also measured as a function of QD charging (Figure 7). The PL decay at V_A is multiexponential (Figure 7, inset), with a slow component comparable to that of the colloidal Mn^{2+}:CdS QDs ($\tau_{Mn} = 1.4$ ms, Supporting Information). Faster contributions are also observed, attributable to nonradiative relaxation processes. The decay constant of the slow component in Figure 7(inset) is essentially independent of applied potential between V_A and V_B, despite the overall decrease in PL intensity by ~98% over this range (Figure 4b). This result indicates that some Mn^{2+} ions are unaffected by partial charging of the QD film, while others are deactivated on submillisecond time scales. The main panel of Figure 7 shows the same time-resolved PL data over a shorter time window, now normalized at 5 ms to emphasize changes at shorter times. These data reveal a short-time scale nonradiative Mn^{2+} decay channel

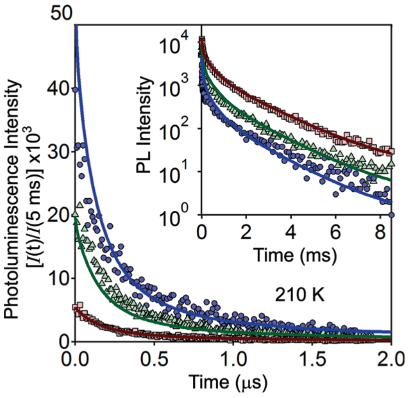

Figure 7. Voltage dependence of the Mn^{2+} photoluminescence decay times. 210 K photoluminescence time dependence for a Mn^{2+}:CdS QD film held at V_A (red solid square) and at two potentials more negative than V_B corresponding to 65% (green triangle) and 80% (black solid circle) bleach of the steady-state photoluminescence intensity. The curves have been normalized to the value at 5 ms to emphasize short-time dynamics. (Inset) Semilog plot of the same data over a broader time scale. These data have not been normalized. The similar Mn^{2+} PL intensities at $t \approx 0$ ns indicates that quenching occurs after Mn^{2+} excitation. The solid lines show photoluminescence decay curves calculated using the model described in the text and parameters from fits of steady-state absorption and photoluminescence data (see text).

growing in with QD charging. As shown below, these time-resolved PL results are precisely what should be expected from e^-_{CB}-Mn^{2+} Auger de-excitation.

Kinetic Model. The sharp contrast between the absorption and PL responses in Figures 4, 5a, and 6, and that between the PL responses of doped and undoped QDs (Figure 5c), both reflect the fact that absorption spectroscopy probes instantaneous charging levels, whereas PL spectroscopy is sensitive to dynamical processes. The results above were therefore analyzed using a kinetic model in which Mn^{2+} excited-state decay is described by an effective decay rate constant (k_{eff}) having contributions from both charge-independent (intrinsic) and charge-dependent (Auger) processes:[64,65]

$$k_{eff}(E_{CB},V) = k_{Mn} + k_{Aug}\rho_{e^-}(E_{CB},V) \qquad (1)$$

Here, k_{Mn} is the Mn^{2+} ${}^4T_1 \rightarrow {}^6A_1$ total decay rate constant (radiative plus nonradiative) in the absence of additional electrons, and k_{Aug} is the nonradiative Auger de-excitation rate constant (approximated to be size independent over the range of diameters in this ensemble). $\rho_{e^-}(E_{CB},V)$ describes the average number of CB electrons per QD for the subset of QDs having $1S_e$ energies of E_{CB}, when the system is held at potential V. $\rho_{e^-}(E_{CB},V)$ can take values of 0–2.

The possibility that the apparent Mn^{2+} PL quenching could stem from electron-exciton (negative trion) Auger de-excitation occurring before energy transfer to Mn^{2+}, instead of from electron-Mn^{2+} Auger de-excitation occurring after energy transfer to Mn^{2+}, can be eliminated on the basis of two key observations. First, the Mn^{2+} PL intensity immediately after the excitation pulse is not reduced upon charge injection (see Figure 7(inset), $t \approx 0$ ns), indicating that Mn^{2+} sensitization proceeds independent of the charge state of the film within this experimental range. This observation demonstrates that PL quenching occurs *after* Mn^{2+} excitation. These dynamics are consistent with reports of exciton-to-Mn^{2+} energy transfer times that are at least 50 times faster than electron-exciton Auger de-excitation times.[36,41] Second, Mn^{2+} PL is substantially quenched even when the number of electrons per QD is small (see Figure 5c), that is, when the probability of photoexciting a QD that already contains an electron is small. Electron-exciton Auger de-excitation therefore cannot be responsible for the Mn^{2+} PL quenching observed here.

$\rho_{e^-}(E_{CB},V)$ can be determined experimentally by modeling the QD absorption bleach with charging.[61] In the limit of fast electron diffusion, $\rho_{e^-}(E_{CB},V)$ is governed by Fermi-Dirac statistics as described by eq 2, where E_{CB} is the CB potential, k_B is the Boltzmann constant, T is the temperature, and $g_{1S_e} = 2$ is the multiplicity of the $1S_e$ level. The energy (E_{rep}) associated with adding an electron to a QD with a charged neighbor, and with adding a second electron to a QD, is described by eq 3,[61] where e is the elementary charge, ε is the dielectric constant of the QD film, ε_0 is the permittivity of vacuum, and λ accounts for electrolyte screening.[61] J_{ee} describes the average Coulomb energy associated with introducing a second electron into a QD ($J_{ee} = 0$ for $\rho_{e^-}(E_{CB},V) \leq 1$, and >0 for $\rho_{e^-}(E_{CB},V) > 1$).[61,66]

$$\rho_{e^-}(E_{CB},V) = \frac{g_{1S_e}}{1+\exp\left(\frac{E_{CB}+E_{rep}-V}{k_BT}\right)} \qquad (2)$$

$$E_{rep}(E_{CB},V) = (1-\lambda)\frac{3eN_{e^-}^{1/3}}{d_{QD}\pi\varepsilon\varepsilon_0} + (\rho(E_{CB},V)-1)J_{ee} \qquad (3)$$

Within this model, $\Delta A(V)/A_0$ can be calculated using eq 4, where the second term accounts for inhomogeneous broadening of E_{CB} due to the finite QD size distribution and surface effects. Using $d_{QD} = 4.5$ nm and parameters similar to those found for undoped QD films ($J_{ee} = 85$ meV, $\lambda = 0.92$, and $\varepsilon = 30$ estimated from the solvent, ligands, and counterions[61]), eq 4 reproduces the experimental $\Delta A(V)/A_0$ data well for $E_0 = -1.15$ eV and $\sigma = 0.14$ eV (Figure 8a).

$$\frac{\Delta A(V)}{A_0} = -\int \frac{1}{2}\rho_{e^-}(E_{CB},V) \times \frac{\exp\left(\frac{-(E_{CB}-E_0)^2}{2\sigma^2}\right)}{\sigma\sqrt{2\pi}}\, dE_{CB} \qquad (4)$$

With $\rho_{e^-}(E_{CB},V)$ defined by the absorption measurement, the steady-state PL intensity at any given electrochemical potential can now be analyzed using eq 1, where k_{Aug} is the only unknown parameter. For

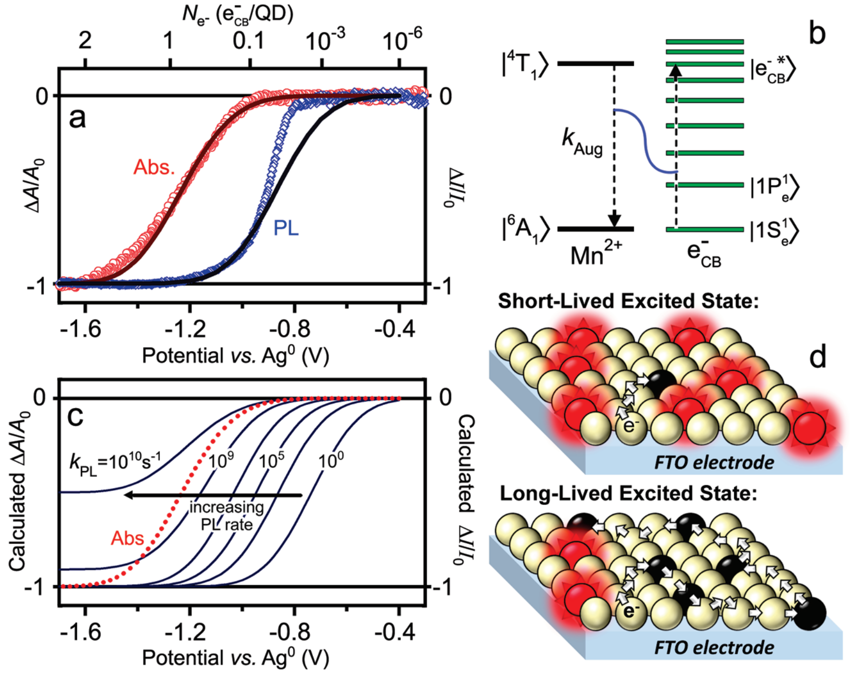

Figure 8. Modeling Auger de-excitation in Mn^{2+}:CdS QD films. (a) Experimental $\Delta A/A_0$ (red open circle) and $\Delta I/I_0$ (open diamond) as a function of applied potential, from Figure 4. The solid lines show calculated absorption and PL responses to nanocrystal charging as described in the text. This analysis yields $k_{Aug} = 0.5 \times 10^{10}$ s^{-1}(e$^-$/QD)$^{-1}$ (2.5×10^{-10} cm^3 s^{-1}). See text for details. (b) Schematic representation of the e^-_{CB}-Mn^{2+} Auger de-excitation in Mn^{2+}:CdS QDs. Nonradiative energy transfer deactivates the Mn^{2+} $^4T_1$ state and promotes a $1S_e$ electron to a highly excited state. The process is energy conserving. (c) Calculated absorption ($\Delta A/A_0$, dashed red) and PL ($\Delta I/I_0$, solid blue) *vs* potential curves for various excited-state decay rate constants, k_{PL} (10^{10}, 10^9, 10^7, 10^5, 10^3, and 10^0 s^{-1}). Decreasing k_{PL} increases sensitivity of the film to Auger de-excitation. Undoped semiconductor nanocrystals frequently show PL decay rate constants on the order of 10^9 s^{-1}, compared to $\sim 10^3$ s^{-1} for Mn^{2+}. (d) Schematic illustration of the role of excited-state lifetimes in Auger de-excitation of undoped and Mn^{2+}-doped QD films. Red spheres represent photoexcited QDs, and black spheres represent those that have undergone Auger de-excitation. The arrows represent the electron's diffusion path. Because the Mn^{2+} excited-state lifetime in the doped QD film is $\sim 10^5$ times longer than the exciton lifetime in the undoped QD film, the electron can sample more of the doped QD film on the time scale of the excited-state decay, thus making Auger de-excitation more competitive with PL.

example, at the potential where the Mn^{2+} PL is quenched 50% ($\Delta I/I_0 = -0.5$), $k_{Mn} = k_{Aug}\rho_{e^-}(E_{CB},V)$ from eq 1. Using $\rho_{e^-}(E_{CB},V)$ at this potential determined from Figure 8a and the experimental PL time dependence at V_A, a value of $k_{Aug} \approx 0.2 \times 10^{10}$ s^{-1}(e$^-$/QD)$^{-1}$ is estimated. Interestingly, $\rho_{e^-}(E_{CB},V)$ at this potential corresponds to $\sim$25 QDs per CB electron; that is, *each CB electron must quench multiple photoexcited QDs*. For comparison with literature values, k_{Aug} is converted to units of cm^3 s^{-1} (per e$^-$), yielding $k_{Aug} = 1.0 \times 10^{-10}$ cm^3 s^{-1}. Auger rate constants of 5×10^{-10} cm^3 s^{-1} and between 4×10^{-10} and 20×10^{-10} cm^3 s^{-1} have been reported for bulk Mn^{2+}:ZnSe and Mn^{2+}:ZnS, respectively,[64,65] and 8×10^{-15} cm^3 s^{-1} has been reported for bulk Mn^{2+}:CdF$_2$.[9] The value of k_{Aug} measured here for Mn^{2+}-doped nanocrystals thus agrees well with literature values measured for Mn^{2+}-doped bulk semiconductors. We note that these previous measurements have all used temperature to vary electron concentrations. The electrochemical approach here excels in providing fine control over electron concentrations.

The $\Delta I(V)/I_0$ curve of Figure 4d can also be simulated using eq 5. With a similar value for k_{Aug} (0.5×10^{10} s^{-1}(e^-_{CB}/QD)$^{-1}$, or 2.5×10^{-10} cm^3 s^{-1}), eq 5 reproduces the experimental data well at all but the lowest electron concentrations ($\sim 10^{-8} < N_{e^-} < \sim 0.05$ e^-_{CB}/QD, Figure 8a), where it predicts greater quenching than observed experimentally. Below a critical value of N_{e^-}, the added electrons cannot sample the entire QD film on the time scale of the Mn^{2+} excited-state decay, despite adequate thermal energy, and the assumption underpinning eq 2 that electron distributions are simply dictated by Fermi-Dirac statistics breaks down. In the low-charging regime, Auger de-excitation rates (and hence PL intensities) are determined by electron mobilities. This conclusion is supported by previous reports of extremely small electron mobilities in this regime.[62,67−69]

$$\frac{I(V)}{I_0} = \int \frac{k_{Mn}}{k_{Mn} + k_{Aug}\rho_{e^-}(E_{CB}, V)} \times \frac{\exp\left(\frac{-(E_{CB} - E_0)^2}{2\sigma^2}\right)}{\sigma\sqrt{2\pi}}\, dE_{CB} \qquad (5)$$

As an independent test of the above analysis, the same model and fitting parameters were used to predict the PL time dependence as a function of QD charging. Equation 6 describes the time-dependent PL intensities as a function of V. Using fixed parameters from Figure 8a and the experimental PL decay curve at V_A in place of the single-exponential decay implied by eq 6, decay curves at other potentials were calculated and compared with experimental data in Figure 7. The PL quenching dynamics are reproduced remarkably well, particularly considering that these calculations involved no adjustable parameters. This excellent agreement strongly supports the above analysis.

$$I(V,t) = \int \exp(-[k_{Mn} + k_{Aug}\rho_{e^-}(E_{CB},V)]t) \times \frac{\exp(\frac{-(E_{CB} - E_0)^2}{2\sigma^2})}{\sigma\sqrt{2\pi}} \mathrm{d}E_{CB} \qquad (6)$$

Microscopic Origins of the Highly Effective Auger De-excitation. The results presented above reveal highly effective Auger de-excitation of dopants by CB electrons in Mn^{2+}-doped semiconductor nanocrystals. Such effective Auger de-excitation of Mn^{2+} is remarkable because of the highly localized nature of the Mn^{2+} d–d transition involved, as it implies strong interaction between localized Mn^{2+} d electrons and delocalized CB electrons. It is therefore of considerable interest and importance to understand why this e^-_{CB}-Mn^{2+} Auger de-excitation is so effective.

Electron-Mn^{2+} Auger de-excitation can be described microscopically as energy transfer from an excited Mn^{2+} ion to a CB electron (Figure 8b), followed by relaxation of the hot electron *via* phonon emission. k_{Aug} can thus be expressed in the general form of Fermi's golden rule eq 7.[1,65] The initial state in eq 7 corresponds to the $^4T_1$ excited state of Mn^{2+} coupled to the CB electron in its $1S_e$ ground electronic state, denoted here as $|i\rangle = |^4T_1, 1S_e^1\rangle$. The state formed by the Auger process involves ground-state Mn^{2+} ($^6A_1$) coupled to a highly excited conduction band electron, denoted $\langle f| = \langle ^6A_1, e^-_{CB}{}^*|$. For conservation of energy, the electron's excited state must lie ~2.1 eV above its $1S_e$ state. $r(E)$ describes the density-of-states (DOS)-weighted overlap factor.

$$k_{Aug} = \frac{2\pi}{\hbar}|\langle f|H'|i\rangle|^2 r(E) \qquad (7)$$

As noted previously,[1] the matrix elements $\langle f|H'|i\rangle$ are similar to those describing the s–d exchange, which contributes, for example, to the giant excitonic Zeeman splittings observed by MCD in Figure 2c. Qualitatively, it can be postulated that k_{Aug} is related to s–d exchange as the exciton-to-Mn^{2+} energy-transfer rate constant (k_{ET}) is related to the sum of s–d and p–d exchange contributions. Values of $k_{ET} = 10^{10}$–10^{12} s^{-1} (per Mn^{2+}) have been measured in various doped semiconductor nanostructures.[36,51–53] Given that the s–d exchange is ~9 times weaker than the p–d exchange in bulk Mn^{2+}:CdS,[70] $k_{Aug} \approx 2.5 \times 10^{10}$ s^{-1} $(e^-/QD)^{-1}$ is a reasonable order of magnitude for a process mediated by s–d exchange.

The dominant orbital interaction behind this s–d exchange is hybridization between the CB-edge and empty Mn^{2+}(4s) orbitals.[71] The location of the participating Mn^{2+}(4s) orbital only ~2.4 eV above the bulk CdS CB edge[71] is conducive to Mn^{2+}(4s)-CB hybridization throughout the CB width. A DOS valley (X point) also resides ~2 eV above the CB edge in bulk CdS, providing ample energy conserving pathways for Auger de-excitation of Mn^{2+} to form $e^-_{CB}{}^*$,[1,72] even though such $e^-_{CB}{}^*$ states aren't observed spectroscopically at 2.1 eV above the $1S_e$ ground state (because of small oscillator strengths). The large Auger de-excitation rate constant in Mn^{2+}-doped CdS QDs is thus understood in terms of substantial Mn^{2+}(4s)-CB hybridization (large $\langle f|H'|i\rangle$) and a large density of e^-_{CB} excited states ~2.1 eV above the $1S_e$ state (large $r(E)$).

The large k_{Aug} alone cannot explain the significantly greater sensitivity of Mn^{2+} PL to Auger de-excitation than seen for excitonic PL in undoped QDs (Figure 5c), however. The e^-_{CB}-Mn^{2+} Auger rate constant found here (2.5×10^{-10} $cm^3 s^{-1}$) is in fact essentially indistinguishable from that reported for $e^-_{CB}{}^*$-exciton (negative trion) Auger relaxation in undoped semiconductor nanocrystals (0.88×10^{-10} cm^3 s^{-1} for CdSe/CdS QDs,[41] see Supporting Information). To understand this most prominent qualitative difference between Mn^{2+}-doped and undoped QDs, the important role of excited-state lifetime must be acknowledged. As seen from eq 1, Auger de-excitation competes against intrinsic relaxation. Modification of the PL decay kinetics therefore alters the competitiveness of the Auger quenching process.

Figure 8c shows simulated PL *versus* potential curves calculated as a function of PL rate constant (replacing k_{Mn} in eq 1 with k_{PL}) using the same model and parameters outlined above. This figure shows that the voltage difference between absorption and PL response curves is a function of excited-state PL decay time. Increasing k_{PL} shifts the PL quenching to more negative potentials. Excitonic PL in many undoped QDs decays with $k_{PL} \approx 10^9$ s^{-1}, and the PL quenching curve for this rate constant reproduces the general experimental observations[41,58] of Auger de-excitation for such QDs, showing near coincidence of absorption bleach and PL quenching, and incomplete PL quenching even after complete filling of the $1S_e$ shell. More quantitatively, the dashed line in Figure 5c shows the quenching predicted for undoped CdSe/CdS QDs, calculated using the above model and the reported values of $k_{ex} = 3.4 \times 10^9$ s^{-1} (ref 58) and $k_{Aug} = 0.88 \times 10^{-10}$ cm^3 s^{-1} (ref 41), with all other parameters fixed at the values used to simulate the Mn^{2+}:CdS QD data (see Supporting Information). The calculated and experimental results agree very well.

This analysis demonstrates that the exceptionally effective Auger de-excitation of Mn^{2+}-doped QDs is primarily attributable to the very long Mn^{2+}

excited-state lifetime, which makes Auger de-excitation kinetically highly competitive according to eq 1.[73] This kinetic competition is summarized schematically in Figure 8d, which illustrates less effective Auger de-excitation of short-lived excited states because of the smaller volume sampled by the CB electron on the excited-state decay time scale.

CONCLUSION

Complete and reversible quenching of Mn^{2+}-doped CdS QD photoluminescence has been achieved through reversible introduction of CB electrons into these QDs by electrochemical methods. The data show that these Mn^{2+}-doped QDs are far more sensitive to Auger quenching than their undoped QD analogues. This remarkably effective Auger de-excitation is understood in terms of energy transfer from Mn^{2+} in its $^4T_1$ excited state to a CB electron, enabled by strong s−d exchange, a large density of acceptor states at the correct energies, and in particular the long Mn^{2+} excited-state lifetime. The large voltage difference between absorption and PL responses of the Mn^{2+}:CdS QDs is primarily a consequence of the very long Mn^{2+} excited-state lifetime. The striking sensitivity of Mn^{2+}-doped nanocrystal PL to Auger quenching strongly suggests that the impact of Auger processes on studies of blinking[25,31] or high-power photoexcitation[35−37] of doped semiconductor nanocrystals should be exacerbated compared to undoped nanocrystals. Such effective Auger de-excitation could also define the fundamental limits of doped-nanocrystal-based electroluminescent devices.[4−8]

The deviation from the thermal equilibrium model observed at very low electron concentrations ($\sim10^{-8} < N_{e^-} < \sim0.05\ e^{-}_{CB}$/QD) is also interesting. This deviation suggests that Auger de-excitation of Mn^{2+} PL could potentially provide a useful optical measure of electron mobilities in other QD films at such low carrier densities, where the usual methods are limited.[62,68] For example, QD Schottky junction solar cells[74] constitute an important class of devices where detailed information about mobilities at very low carrier densities (*e.g.*, under ambient illumination) would be desirable. Electron-Mn^{2+} Auger quenching has been used for imaging charge carriers in semiconductor devices previously, allowing demonstration of spatial separation of the acceleration and impact excitation processes in high-field electroluminescence devices made from bulk Mn^{2+}:CaF_2.[9] With this precedent, the demonstration here of effective Auger de-excitation in Mn^{2+}-doped QD films suggests that Auger-based imaging might now be accessible in QD devices. This proposed application could be extended to other colloidal doped nanocrystal films with long-lived electronic excited states, such as Er^{3+}-doped colloidal Si nanocrystals.

Finally, the ability to quench Mn^{2+} PL so effectively with very few electrons may provide a mechanism for switching Mn^{2+} PL on time scales shorter than its intrinsic PL decay time, which would normally define the lower limit. In QD films, this possibility would rely on charge injection and diffusion being fast relative to Mn^{2+} PL decay. Experiments are presently underway to explore this possibility.

METHODS

Synthesis and Characterization. Colloidal Mn^{2+}:CdS QDs were synthesized by modification of a method reported previously,[26] and stored as suspensions in toluene. Films of Mn^{2+}:CdS QDs were prepared according to literature methods[41,57,58] by depositing QD suspensions onto a 3-mercaptopropyl-trimethoxysilane treated FTO surface, dipping the QDs in a solution of 1,7-heptanediamine in EtOH for ∼1 min, heating the resulting film at 70 °C for between 0.5 and 3.0 h, and finally vacuum curing for 1 h (see Supporting Information for complete details).

Electrochemistry. The electrochemical cells were assembled under N_2 atmosphere using a platinum wire as a counter-electrode and a silver wire as a pseudoreference electrode in a 0.1 M solution of tetrabutylammonium perchlorate (TBAP) in dimethylformamide (DMF).[56−58] All electrochemical measurements were done at 210 K in a flow cryostat under N_2 atmosphere. A μ-autolab II potentiostat was used to control the potential and record the current in linear sweep and cyclic voltammetry modes.

Spectroscopy. Absorption measurements were performed on colloidal suspensions of QDs in toluene at 295 K and on QD films at 210 K using a Cary 500 (Varian) spectrometer. All PL data were collected using a 0.5 m monochromator. PL spectra were collected using CCD detection. PLE and time-resolved PL measurements were performed with PMT detection fixed at 585 nm (25 nm spectral band-pass). All PL measurements involved excitation well above the band edge to minimize changes in excitation density due to absorption bleaching, and at low excitation densities to avoid any nonlinear effects. QYs were measured using an integrating sphere. MCD spectra were collected using an Aviv 40DS spectropolarimeter and a 7 T superconducting magneto-optical cryostat (Cryo-Industries) positioned in the Faraday configuration (see Supporting Information for additional details).

Acknowledgment. This work was supported by the US National Science Foundation (DMR-0906814 to D.R.G.). M.A.W. thanks the Center for Nanotechnology at the University of Washington for UIF fellowship support. EPR instrumentation support from the Center for Ecogenetics and Environmental Health UW center Grant P30 ES07033 from the National Institutes of Environmental Health Sciences (NIH) is gratefully acknowledged.

Supporting Information Available: Additional experimental details and results. This material is available free of charge *via* the Internet at http://pubs.acs.org.

REFERENCES AND NOTES

1. Allen, J. W. Impact Excitation and Auger Quenching of Luminescent Centers in Crystals, with Special Reference to ZnS−Mn. *J. Phys. C* **1986,** *19*, 6287–6295.
2. Bringuier, E. Impact Excitation in ZnS-Type Electroluminescence. *J. Appl. Phys.* **1991,** *70*, 4505–4512.

3. Bringuier, E. Tentative Anatomy of ZnS-Type Electroluminescence. *J. Appl. Phys.* **1994,** *75*, 4291–4312.
4. Adachi, D.; Hasui, S.; Toyama, T.; Okamoto, H. Structural and Luminescence Properties of Nanostructured ZnS:Mn. *Appl. Phys. Lett.* **2000,** *77*, 1301–1303.
5. Yang, H.; Holloway, P. H. Electroluminescence from Hybrid Conjugated Polymer-CdS:Mn/ZnS Core/Shell Nanocrystals Devices. *J. Phys. Chem. B* **2003,** *107*, 9705–9710.
6. Yang, H.; Holloway, P. H.; Ratna, B. B. Photoluminescent and Electroluminescent Properties of Mn-Doped ZnS Nanocrystals. *J. Appl. Phys.* **2003,** *93*, 586–592.
7. Adachi, D.; Morimoto, T.; Hama, T.; Toyama, T.; Okamoto, H. Orange Electroluminescence from Chemically Synthesized Zinc Sulfide Nanocrystals Doped with Manganese. *J. Non-Cryst. Solids* **2008,** *354*, 2740–2743.
8. Wood, V.; Halpert, J. E.; Panzer, M. J.; Bawendi, M. G.; Bulovic, V. Alternating Current Driven Electroluminescence from ZnSe/ZnS:Mn/ZnS Nanocrystals. *Nano Lett* **2009,** *9*, 2367–2371.
9. Langer, J. M.; Lemanska-Bajorek, A.; Suchocki, A. A Method of Excitation Profiling in High-Field Electroluminescence. *Appl. Phys. Lett.* **1981,** *39*, 386–388.
10. Suchocki, A.; Langer, J. M. Auger Effect in Mn^{2+} Luminecence of CdF_2:(Mn,Y) Crystals. *Phys. Rev. B* **1989,** *39*, 7905–7916.
11. Palm, J.; Gan, F.; Zheng, B.; Michel, J.; Kimerling, L. C. Electroluminescence of Erbium-Doped Silicon. *Phys. Rev. B* **1996,** *54*, 17603–17615.
12. Priolo, F.; Franzo, G.; Coffa, S.; Carnera, A. Excitation and Nonradiative Deexcitation Processes of Er^{3+} in Crystalline Si. *Phys. Rev. B* **1998,** *57*, 4443–4455.
13. Kik, P. G.; Polman, A. Gain Limiting Processes in Er-Doped Si Nanocrystal Waveguides in SiO_2. *J. Appl. Phys.* **2002,** *91*, 534–536.
14. Kik, P. G.; Polman, A. Exciton-Erbium Interactions in Si Nanocrystal-Doped SiO_2. *J. Appl. Phys.* **2000,** *88*, 1992–1998.
15. Maurizio, C.; Iacona, F.; D'Acapito, F.; Franzo, G.; Priolo, F. Er Site in Er-Implanted Si Nanoclusters Embedded in SiO_2. *Phys. Rev. B* **2006,** *74*, 205428.
16. Beaulac, R.; Ochsenbein, S. T.; Gamelin, D. R. Colloidal Transition-Metal-Doped Quantum Dots, in *Nanocrystal Quantum Dots: Synthesis and Electronic and Optical Properties*; Klimov, V. I., Ed.; Taylor & Francis: London, 2010.
17. Suyver, J. F.; Wuister, S. F.; Kelly, J. J.; Meijerink, A. Luminescence of Nanocrystalline ZnSe:Mn^{2+}. *Phys. Chem. Chem. Phys.* **2000,** *2*, 5445–5448.
18. Norris, D. J.; Yao, N.; Charnock, F. T.; Kennedy, T. A. High-Quality Manganese-Doped ZnSe Nanocrystals. *Nano Lett.* **2001,** *1*, 3–7.
19. Schwartz, D. A.; Norberg, N. S.; Nguyen, Q. P.; Parker, J. M.; Gamelin, D. R. Magnetic Quantum Dots: Synthesis, Spectroscopy, and Magnetism of Co^{2+}- and Ni^{2+}-Doped ZnO Nanocrystals. *J. Am. Chem. Soc.* **2003,** *125*, 13205–13218.
20. Archer, P. I.; Santangelo, S. A.; Gamelin, D. R. Inorganic Cluster Syntheses of TM^{2+}-Doped Quantum Dots (CdSe, CdS, CdSe/CdS): Physical Property Dependence on Dopant Locale. *J. Am. Chem. Soc.* **2007,** *129*, 9808–9818.
21. Archer, P. I.; Santangelo, S. A.; Gamelin, D. R. Direct Observation of sp−d Exchange Interactions in Colloidal Mn^{2+}- and Co^{2+}-Doped CdSe Quantum Dots. *Nano Lett.* **2007,** *7*, 1037–1043.
22. Pradhan, N.; Peng, X. Efficient and Color-Tunable Mn-Doped ZnSe Nanocrystal Emitters: Control of Optical Performance *via* Greener Synthetic Chemistry. *J. Am. Chem. Soc.* **2007,** *129*, 3339–3347.
23. Beaulac, R.; Archer, P. I.; van Rijssel, J.; Meijerink, A.; Gamelin, D. R. Exciton Storage by Mn^{2+} in Colloidal Mn^{2+}-Doped CdSe Quantum Dots. *Nano Lett.* **2008,** *8*, 2949–2953.
24. Beaulac, R.; Archer, P. I.; Liu, X.; Lee, S.; Salley, G. M.; Dobrowolska, M.; Furdyna, J. K.; Gamelin, D. R. Spin-Polarizable Excitonic Luminescence in Colloidal Mn^{2+}-Doped CdSe Quantum Dots. *Nano Lett.* **2008,** *8*, 1197–1201.
25. Zhang, Y. P.; Gan, C. L.; Muhammad, J.; Battaglia, D.; Peng, X. G.; Xiao, M. Enhanced Fluorescence Intermittency in Mn-Doped Single ZnSe Quantum Dots. *J. Phys. Chem. C* **2008,** *112*, 20200–20205.
26. Nag, A.; Chakraborty, S.; Sarma, D. D. To Dope Mn^{2+} in a Semiconducting Nanocrystal. *J. Am. Chem. Soc.* **2008,** *130*, 10605–10611.
27. Beaulac, R.; Schneider, L.; Archer, P. I.; Bacher, G.; Gamelin, D. R. Light-Induced Spontaneous Magnetization in Doped Colloidal Quantum Dots. *Science* **2009,** *325*, 973–976.
28. Bussian, D. A.; Crooker, S. A.; Yin, M.; Brynda, M.; Efros, Al. L.; Klimov, V. I. Tunable Magnetic Exchange Interactions in Manganese-Doped Inverted Core−Shell ZnSe−CdSe Nanocrystals. *Nat. Mater.* **2009,** *8*, 35–40.
29. Vlaskin, V. A.; Beaulac, R.; Gamelin, D. R. Dopant-Carrier Magnetic Exchange Coupling in Inverted Core/Shell Nanocrystals. *Nano Lett.* **2009,** *9*, 4376–4382.
30. Ochsenbein, S. T.; Feng, Y.; Whitaker, K. M.; Badaeva, E.; Liu, W. K.; Li, X.; Gamelin, D. R. Charge-Controlled Magnetism in Colloidal Doped Semiconductor Nanocrystals. *Nat. Nanotechnol.* **2009,** *4*, 681–687.
31. Ishizumi, A.; Kanemitsu, Y. Blinking Behavior of Surface-Defect and Impurity Luminescence in Nondoped and Mn^{2+}-Doped CdS Nanocrystals. *J. Phys. Soc. Jpn.* **2009,** *78*, 083705.
32. Yu, J. H.; Liu, X.; Kweon, K. E.; Joo, J.; Park, J.; Ko, K.-T.; Lee, D. W.; Shen, S.; Tivakornsasithorn, K.; Son, J. S.; *et al.* Giant Zeeman Splitting in Nucleation-Controlled Doped CdSe: Mn^{2+} Quantum Nanoribbons. *Nat. Mater.* **2010,** *9*, 47–53.
33. Vlaskin, V. A.; Janssen, N.; van Rijssel, J.; Beaulac, R.; Gamelin, D. R. Tunable Dual Emission in Doped Semiconductor Nanocrystals. *Nano Lett.* **2010,** *10*, 3670–3674.
34. Li, Z.; Cheng, L.; Sun, Q.; Zhu, Z.; Riley, M. J.; Aljada, M.; Cheng, Z.; Wang, X.; Hanson, G. R.; Qiao, S.; *et al.* Diluted Magnetic Semiconductor Nanowires Prepared by the Solution−Liquid−Solid Method. *Angew. Chem.* **2010,** *49*, 2777–2781.
35. Chen, O.; Shelby, D. E.; Yang, Y.; Zhuang, J.; Wang, T.; Niu, C.; Omenetto, N.; Cao, Y. C. Excitation-Intensity-Dependent Color-Tunable Dual Emissions from Manganese-Doped CdS/ZnS Core/Shell Nanocrystals. *Angew. Chem., Int. Ed.* **2010,** *49*, 10132–10135.
36. Chen, H.-Y.; Chen, T.-Y.; Son, D. H. Measurement of Energy Transfer Time in Colloidal Mn-Doped Semiconductor Nanocrystals. *J. Phys. Chem. C* **2010,** *114*, 4418–4423.
37. Taguchi, S.; Ishizumi, A.; Kanemitsu, Y. Multicarrier Recombination and Energy Transfer in Mn-Doped CdS Nanocrystals Studied by Femtosecond Pump−Probe Spectroscopy. *J. Phys. Soc. Jpn.* **2010,** *79*, 063710.
38. Zu, L. J.; Wills, A. W.; Kennedy, T. A.; Glaser, E. R.; Norris, D. J. Effect of Different Manganese Precursors on the Doping Efficiency in ZnSe Nanocrystals. *J. Phys. Chem. C* **2010,** *114*, 21969–21975.
39. Ochsenbein, S. T.; Gamelin, D. R. Quantum Oscillations in Magnetically Doped Colloidal Nanocrystals. *Nat. Nanotechnol.* **2011,** *6*, 112–115.
40. Carreras, J.; Bonafos, C.; Montserrat, J.; Dominguez, C.; Arbiol, J.; Garrido, B. Auger Quenching-Based Modulation of Electroluminescence from Ion-Implanted Silicon Nanocrystals. *Nanotechnology* **2008,** *19*, 205201.
41. Jha, P. P.; Guyot-Sionnest, P. Trion Decay in Colloidal Quantum Dots. *ACS Nano* **2009,** *3*, 1011–1015.
42. Klimov, V. I.; McGuire, J. A.; Schaller, R. D.; Rupasov, V. I. Scaling of Multiexciton Lifetimes in Semiconductor Nanocrystals. *Phys. Rev. B* **2008,** *77*, 195324.
43. Wehrenberg, B. L.; Wang, C. J.; Guyot-Sionnest, P. Interband and Intraband Optical Studies of PbSe Colloidal Quantum Dots. *J. Phys. Chem. B* **2002,** *106*, 10634–10640.
44. Efros, A. L.; Rosen, M. Random Telegraph Signal in the Photoluminescence Intensity of a Single Quantum Dot. *Phys. Rev. Lett.* **1997,** *78*, 1110–1113.
45. Frantsuzov, P.; Kuno, M.; Janko, B.; Marcus, R. A. Universal Emission Intermittency in Quantum Dots, Nanorods and Nanowires. *Nat. Phys.* **2008,** *4*, 519–522.
46. Zhao, J.; Nair, G.; Fisher, B. R.; Bawendi, M. G. Challenge to the Charging Model of Semiconductor-Nanocrystal Fluorescence Intermittency from Off-State Quantum Yields and Multiexciton Blinking. *Phys. Rev. Lett.* **2010,** *104*, 157403.

47. Krauss, T. D.; Peterson, J. J. Bright Future for Fluorescence Blinking in Semiconductor Nanocrystals. *J. Phys. Chem. Lett.* **2010,** *1*, 1377–1382.
48. Rosen, S.; Schwartz, O.; Oron, D. Transient Fluorescence of the Off State in Blinking CdSe/CdS/ZnS Semiconductor Nanocrystals is Not Governed by Auger Recombination. *Phys. Rev. Lett.* **2010,** *104*, 157404.
49. The ubiquitous exciton-to-dopant energy transfer process that gives rise to sensitized dopant PL is sometimes also described as an Auger process. (see for example: Chernenko, A. V.; Brichkin, A. S.; Sobolev, N. A.; Carmo, M. C. Mechanisms of Manganese-Assisted Nonradiative Recombination in Cd(Mn)Se/Zn(Mn)Se Quantum Dots *J. Phys.-Cond. Matter.* 2010, *22*, 355306.) We refer here specifically to Auger de-excitation (*i.e.*, dopant PL quenching) processes.
50. Yu, W. W.; Qu, L.; Guo, W.; Peng, X. G. Experimental Determination of the Extinction Coefficient of CdTe, CdSe, and CdS Nanocrystals. *Chem. Mater.* **2003,** *15*, 2854–2860.
51. Chung, J. H.; Ah, C. S.; Jang, D.-J. Formation and Distinctive Decay Times of Surface- and Lattice-Bound Mn^{2+} Impurity Luminescence in ZnS Nanoparticles. *J. Phys. Chem. B* **2001,** *105*, 4128–4132.
52. Toropov, A. A.; Sorokin, S. V.; Kuritsyn, K. A.; Ivanov, S. V.; Pozina, G.; Bergman, J. P.; Wagner, M.; Chen, W. M.; Monemar, B.; Waag, A.; *et al.* Magneto-photoluminescence Studies of Cd(Mn)Se/Zn(Mn)Se Diluted Magnetic Nanostructures. *Physica E* **2001,** *10*, 362–367.
53. Seufert, J.; Bacher, G.; Scheibner, M.; Forchel, A.; Lee, S.; Dobrowolska, M.; Furdyna, J. K. Dynamical Spin Response in Semimagnetic Quantum Dots. *Phys. Rev. Lett.* **2002,** *88*, 027402.
54. Dorain, P. B. Electron Paramagnetic Resonance of Manganese (II) in Hexagonal Zinc Oxide and Cadmium Sulfide Single Crystals. *Phys. Rev.* **1958,** *112*, 1058–1060.
55. Furdyna, J. K. Diluted Magnetic Semiconductors. *J. Appl. Phys.* **1988,** *64*, R29–R64.
56. Haram, S. K.; Quinn, B. M.; Bard, A. J. Electrochemistry of CdS Nanoparticles: A Correlation Between Optical and Electrochemical Band Gaps. *J. Am. Chem. Soc.* **2001,** *123*, 8860–8861.
57. Guyot-Sionnest, P.; Wang, C. M. Fast Voltammetric and Electrochromic Response of Semiconductor Nanocrystal Thin Films. *J. Phys. Chem. B* **2003,** *107*, 7355–7359.
58. Jha, P. P.; Guyot-Sionnest, P. Photoluminescence Switching of Charged Quantum Dot Films. *J. Phys. Chem. C* **2007,** *111*, 15440–15445.
59. Wehrenberg, B. L.; Guyot-Sionnest, P. Electron and Hole Injection in PbSe Quantum Dot Films. *J. Am. Chem. Soc.* **2003,** *125*, 7806–7807.
60. Bard, A. J.; Faulkner, L. R. *Electrochemical Methods: Fundamentals and Applications*, 2nd ed.; John Wiley & Sons, Inc.: New York, 2001.
61. Houtepen, A. J.; Vanmaekelbergh, D. Orbital Occupation in Electron-Charged CdSe Quantum-Dot Solids. *J. Phys. Chem. B* **2005,** *109*, 19634–19642.
62. Yu, D.; Wang, C.; Guyot-Sionnest, P. n-Type Conducting CdSe Nanocrystal Solids. *Science* **2003,** *300*, 1277–1280.
63. The relative magnitude of the trap emission appears to depend on the duration of the heating step in the QD cross-linking process, with less trap emission usually observed for shorter heating times.
64. Gordon, N. T.; Allen, J. W. Auger Quenching of Luminescence in ZnS:Mn. *Solid State Commun.* **1981,** *37*, 441–443.
65. Ayling, S. G.; Allen, J. W. Auger Quenching of Luminescence in ZnSe:Mn. *J. Phys. C. Solid State Phys.* **1987,** *20*, 4251–4257.
66. Lannoo, M.; Delerue, C.; Allan, G. Screening in Semiconductor Nanocrystallites and Its Consequences for Porous Silicon. *Phys. Rev. Lett.* **1995,** *74*, 3415–3418.
67. Vanmaekelbergh, D.; Liljeroth, P. Electron-Conducting Quantum Dot Solids: Novel Materials Based on Colloidal Semiconductor Nanocrystals. *Chem. Soc. Rev.* **2005,** *34*, 299–312.
68. Yu, D.; Wehrenberg, B. L.; Jha, P. P.; Ma, J.; Guyot-Sionnest, P. Electronic Transport of n-Type CdSe Quantum Dot Films: Effect of Film Treatment. *J. Appl. Phys.* **2006,** *99*, 104315.
69. Liu, Y.; Gibbs, M.; Puthussery, J.; Gaik, S.; Ihly, R.; Hillhouse, H. W.; Law, M. Dependence of Carrier Mobility on Nanocrystal Size and Ligand Length in PbSe Nanocrystal Solids. *Nano Lett.* **2010,** *10*, 1960–1969.
70. Nawrocki, M.; Lascaray, J. P.; Coquillat, D.; Demianiuk, M. Ion-Carrier Exchange Interaction in $Cd_{1\text{-}x}Mn_xS$. *Mater. Res. Soc. Symp. Proc.* **1987,** *89*, 65–70.
71. Beaulac, R.; Gamelin, D. R. Two-Center Formulation of Mn^{2+}-Electron s−d Exchange Coupling in Bulk and Quantum Confined Diluted-Magnetic Semiconductors. *Phys. Rev. B* **2010,** *82*, 224401.
72. Rohlfing, M.; Kruger, P.; Pollmann, J. Quasiparticle Band Structure of CdS. *Phys. Rev. Lett.* **1995,** *75*, 3489–3492.
73. For the same reason, the less effective quenching of trap PL with charging observed in Figure 4b is consistent with the faster trap PL decay ($k_{PL} \approx 4 \times 10^7\ s^{-1}$, see Supporting Information).
74. Luther, J. M.; Law, M.; Beard, M. C.; Song, Q.; Reese, M. O.; Ellingson, R. J.; Nozik, A. J. Schottky Solar Cells Based on Colloidal Nanocrystal Films. *Nano Lett.* **2008,** *8*, 3488–3492.